„BABEȘ-BOLYAI” UNIVERSITY
Faculty of Physics
Doctoral School of Physics

PhD Thesis Summary

Enhanced Magnetic Properties of Cobalt Ferrite by Substitutions

---

Szatmári Ádám

Scientific Advisor
Prof. Dr. Romulus Tetean

Cluj-Napoca
2025

Table of Contents

Summary

Magnetic nanoparticles ($MNPs$) have attracted growing attention due to their unique properties and wide-ranging applications in biomedicine, data storage, and environmental technology. Among them, cobalt ferrite ($CoFe_2O_4$), a spinel ferrite, stands out for its high coercivity, moderate saturation magnetization, and strong chemical and mechanical stability, making it ideal for magnetic sensing, data recording, and medical uses like hyperthermia. Improving the magnetic performance of $CoFe_2O_4$ remains a key research goal. One approach is substituting cobalt with other divalent ions like Zn^{2+} or Mn^{2+} to alter the spinel structure and magnetic behavior. This thesis explores how such substitutions, using sol-gel and hydrothermal methods, influence the structural, morphological, and magnetic properties of the nanoparticles.

The aim is to create tunable ferrite nanomaterials for advanced applications, addressing the need for adaptable magnetic nanostructures in fields like medicine and electronics, and contributing to the limited comparative data on Zn^{2+} and Mn^{2+}doping effects across different synthesis techniques.

The thesis is structured into several chapters, each addressing a specific aspect of the study:

- Chapter 1 introduces nanoscale concepts inspired by Feynman, emphasizing how reduced particle size increases surface-area-to-volume ratio, boosting chemical reactivity and sensitivity to external fields—key to magnetic nanoparticle behavior.
- Chapter 2 discusses the fundamental concepts of magnetic nanoparticles, focusing on their structural and magnetic properties. It lays the foundation for understanding how variations in particle size and chemical composition influence their overall behavior.
- Chapter 3 details the experimental methods used in this study. It covers both synthesis techniques sol-gel and hydrothermal methods as well as characterization tools including X-ray diffraction, electron microscopy, Raman spectroscopy, and magnetic measurements.
- Chapter 4 presents the experimental results and their analysis:
  - 4.1 investigates the synthesis and characterization of pure $CoFe_2O_4$ nanoparticles prepared by sol-gel and hydrothermal methods.
  - 4.2 examines the effects of substituting cobalt with zinc in $Co_{1-x}Zn_xFe_2O_4$ nanoparticles synthesized via the sol-gel method.
  - 4.3 analyzes the substitution of cobalt with manganese in $Co_{1-x}Mn_xFe_2O_4$ and its influence on structure and magnetism.

Each section provides a summary of the analysis of the structural, morphological, and magnetic properties, and Chapter 4 concludes with a comprehensive overview of all the results.

Chapter 1 General Introduction

The idea of manipulating matter at the atomic level was famously proposed by Richard Feynman in his visionary 1960 lecture, *"There's Plenty of Room at the Bottom."* This speech is widely regarded as the conceptual origin of nanotechnology, a field that has since grown into a cornerstone of modern science and engineering. At the heart of this field lie nanoparticles (NPs) materials with dimensions between 1 and 100 nanometers. Due to their extremely small size, nanoparticles exhibit physical and chemical properties that are dramatically different from their bulk counterparts.

A key factor behind these unique properties is the exceptionally high surface-area-to-volume ratio ($S/V = 3/R$), which increases rapidly as particle size decreases. This elevated ratio means that a significant proportion of atoms reside at or near the surface of the particle, leading to enhanced chemical reactivity. For instance, gold, which is normally inert in bulk form, becomes highly reactive and displays vivid colors when reduced to the nanoscale, due to localized surface plasmon resonance. This optical phenomenon is highly size dependent and arises from collective oscillations of electrons at the nanoparticle surface under light exposure, demonstrating how quantum effects dominate at the nanoscale.

These distinctive properties make nanoparticles useful in a wide variety of applications. In catalysis, their large surface area enhances reaction rates and reduces the need for high temperatures or pressures, making processes more energy-efficient and cost-effective. In medicine, nanoparticles are being used to deliver drugs directly to cancer cells, minimizing side effects and increasing treatment efficacy. They are also employed in hyperthermia-based cancer therapies, bioimaging, and advanced diagnostic platforms, where their small size and surface functionality are critical.

Environmental applications are equally promising. Nanoparticles can adsorb pollutants from air and water, offering efficient and scalable solutions for environmental remediation. In the field of energy, they are integral to the development of next-generation technologies, such as lithium-ion batteries with higher capacity, supercapacitors with faster charging, and solar cells with improved light absorption and conversion efficiency.

However, the rise of nanotechnology is accompanied by several challenges. Potential toxicity and long-term environmental effects of nanoparticles are not yet fully understood, raising concerns about their safe use and disposal. Additionally, producing nanoparticles at industrial scales while maintaining uniformity and quality remains a technical obstacle. Regulatory frameworks for nanoparticle-containing products are still evolving, often lagging behind technological advances. As the field continues to grow, a careful balance must be struck between innovation and risk management to ensure that the full potential of nanotechnology can be realized for the benefit of society.

Chapter 2 Magnetic nanoparticles

From the literature, we saw that magnetic properties in materials fundamentally originate from the behavior of electrons, especially their spin and orbital movements, which produce magnetic moments. Transition metals such as iron and cobalt exhibit ferromagnetism due to unpaired 3d electrons that align via strong exchange interactions. At the nanoscale, magnetic materials display significant deviations in their properties compared to their bulk forms, influenced by factors such as composition, crystal structure, particle size, and cation distribution. Among these, cobalt ferrite nanoparticles have been extensively studied due to their promising magnetic characteristics and wide range of technological applications.

Magnetic nanoparticles, in general, show unique size-dependent behaviors that make them valuable in fields including medicine, data storage, and environmental science. Ferrites, particularly spinel-structured cobalt ferrite, are noted for their high saturation magnetization and thermal stability, which are essential for practical applications. Studies on other ferrites like magnetite, maghemite, nickel, zinc, and manganese ferrites reveal that cation site occupancy and synthesis conditions critically affect their magnetic responses and biocompatibility, with many of these materials being suitable for biomedical applications such as MRI contrast agents and magnetic hyperthermia treatments.

Further research highlights the importance of synthesis methods and surface modifications, such as surfactant use and polymer coatings, in tailoring particle size, magnetic behavior, and biocompatibility. For cobalt ferrite, coatings improve stability and enable combined diagnostic and therapeutic uses. Composite materials combining cobalt ferrite with carbon nanotubes also show enhanced magneto-dielectric properties, expanding their potential in advanced technologies. Overall, the literature underscores a strong relationship between structure, composition, and magnetic performance, guiding ongoing efforts to optimize these nanoparticles for multifunctional applications in medicine, energy, and emerging fields like quantum computing [1].

2.1 Structural properties of magnetic nanoparticles

The structural characteristics of magnetic nanoparticles, including size, shape, crystallinity, surface chemistry, and doping, critically influence their magnetic behavior and suitability for various applications. Among these factors, nanoparticle size is particularly important. When particle size decreases below a critical threshold (e.g., ferrites smaller than 10 nm), nanoparticles exhibit single-domain behavior with uniformly aligned spins, maximizing magnetic moments. Further reduction below this size results in superparamagnetism, where thermal energy overcomes magnetic anisotropy, causing random fluctuations of magnetic moments above the blocking temperature and preventing permanent magnetization. This makes such nanoparticles ideal for applications requiring temporary magnetic responses, such as targeted drug delivery. Larger nanoparticles (above ~30 nm) maintain ferromagnetic or ferrimagnetic behavior with stable remanent magnetization, useful in magnetic separation and data storage.

Nanoparticle shape also significantly affects magnetic properties through shape anisotropy, influencing coercivity, magnetization reversal, and dipole interactions. Elongated nanoparticles, such as rods or nanowires, exhibit enhanced anisotropy and increased coercivity, making them suitable for permanent magnets and magnetic memory devices. The crystalline structure plays a crucial role in magnetic behavior. Cobalt ferrite nanoparticles typically crystallize in an inverse spinel structure, where the distribution of Co^{2+} and Fe^{3+} ions between tetrahedral and octahedral sites leads to ferrimagnetic ordering and strong exchange interactions that enhance saturation magnetization and magnetic stability. Thermal treatment and synthesis methods can alter cation distribution, impacting structural and magnetic properties.

High crystallinity promotes stronger magnetic coupling and higher saturation magnetization by minimizing atomic disorder. X-ray diffraction patterns reflect crystallinity levels, which correlate with magnetic performance. Surface functionalization improves nanoparticle stability, dispersibility, and biocompatibility, especially important for biomedical applications. Functionalization with polymers such as polyethylene glycol enhances circulation time and reduces immune response. Additionally, surface modifications increase catalytic efficiency by enhancing active sites and improve sensing selectivity by enabling specific interactions with target analytes, thereby facilitating sensitive detection and diagnostics [2–5].

2.2 Magnetic properties of magnetic nanoparticles

Magnetic behavior in nanoparticles (NPs) arises from intrinsic electronic properties and structural characteristics, primarily due to the magnetic moments of electrons and their interactions. Magnetization (M) quantifies magnetic moment per unit volume and reflects responses to external magnetic fields and spontaneous ordering below critical temperatures such as the Curie temperature (T_C).

Materials exhibit various types of magnetism characterized by their magnetic susceptibility (χ), which defines the degree of magnetization induced by an external magnetic field. Diamagnetism (negative, small χ) occurs universally due to orbital electron currents opposing the field, independent of temperature. Paramagnetism (positive, small χ) arises from unpaired electron spins aligning weakly with applied fields, with susceptibility inversely proportional to temperature as described by Curie's law ($\chi = C/T$).

Ferromagnetic materials display strong, positive susceptibility and spontaneous magnetization due to exchange interactions aligning atomic moments parallel within domains. Their susceptibility follows the Curie-Weiss law ($\chi = C/(T - \theta)$) and exhibits hysteresis loops indicative of remanence and coercivity, key for permanent magnet applications. The Curie temperature marks the phase transition from ferromagnetic to paramagnetic states.

Antiferromagnetism involves antiparallel alignment of equal magnetic moments, leading to net zero magnetization below the Néel temperature (T_N), while ferrimagnetism features antiparallel moments of unequal magnitude resulting in net magnetization. Both types show temperature-dependent susceptibilities with distinct magnetic transitions.

Nanoparticle magnetism is strongly influenced by size dependent phenomena such as superparamagnetism, where thermal energy overcomes anisotropy barriers, causing rapid flipping of magnetization and eliminating hysteresis below the blocking temperature (T_B).

Magnetic anisotropy, which stabilizes magnetization along preferred directions, is affected by structural and surface factors in nanoparticles. As size decreases, surface contributions become more significant, impacting the overall magnetic behavior.

Magnetic characterization techniques such as Zero-Field Cooling (ZFC) and Field Cooling (FC) are essential for probing the temperature-dependent magnetic behavior of nanoparticles. These methods provide valuable insights into critical magnetic parameters, including the blocking temperature, magnetic phase transitions, and irreversible magnetization effects. Such parameters are particularly significant for tailoring nanoparticles to meet specific performance requirements in applications ranging from biomedicine such as magnetic hyperthermia and targeted drug delivery to high density data storage systems and advanced magnetic sensors [6,7].

A comprehensive understanding of these magnetic behaviors, combined with the ability to systematically tune them through precise control over nanoparticle size, chemical composition, and crystal structure, is key to maximizing their functional efficiency. This tunability enables researchers and engineers to optimize magnetic nanoparticles for a wide spectrum of cutting-edge technological applications, ensuring both enhanced performance and application-specific suitability.

Chapter 3 Experimental methods

Chapter 3 of the thesis outlines the experimental strategies for synthesizing and characterizing cobalt ferrite-based nanoparticles, with emphasis on producing high-purity nanomaterials possessing tailored magnetic properties. The chapter is structured into two main sections: preparation techniques and characterization methods.

3.1 Preparation techniques

Two synthesis methods were employed: sol-gel and hydrothermal (specifically, solvothermal when using ethylene glycol as the solvent).

I. Sol-gel method

The sol-gel process is appreciated for its ability to control composition and particle size with high precision [8]. It involves:

1. **Preparation of the Sol:** Precursors (e.g., metal alkoxides or salts) are dissolved in solvents like Milli-Q water or lower aliphatic alcohols.
2. **Dissolution and Hydrolysis:** Hydrolysis initiates M–O–M bond formation, leading to nanoparticle nucleation.
3. **Control of Particle Growth:** Surfactants or capping agents help maintain colloidal stability and avoid agglomeration.
4. **Gelation:** Sol transitions to gel via polycondensation, strengthening the 3D network.
5. **Drying of gel and Removal of Solvent:** Gels are dried either by ambient (xerogels) or supercritical drying (aerogels), affecting porosity and structure.
6. **Thermal Treatment (Sintering):** Final crystallization and removal of organic residues occur through sintering.

II. Hydrothermal method

This method, involving precursor dissolution in ethylene glycol and reaction at 240 °C in a Teflon-lined autoclave, is suitable for forming monodispersed nanoparticles with uniform size and shape [9]. For example:

$Fe(acac)_3 + Co(acac)_2 + xH_2O + PVP \rightarrow^{T,P} CoFe_2O_4 + Byproducts(acac - H, H_2O)$, where in the reaction used iron, cobalt and PVP as a stabilizer.

3.2 Characterization techniques

The synthesized nanoparticles were thoroughly investigated using multiple complementary techniques:

a) **X-Ray Diffraction:** XRD was used to determine crystallographic phase purity, lattice parameters, and crystallite size. The calculations were based on Bragg's Law and the Debye–Scherrer equation:
Bragg's Law: $n \cdot \lambda = 2 \cdot d \cdot sin\theta$
Debye-Scherrer: $D = K \cdot \lambda \, / \, (\beta \ \cdot cos\theta)$
These analyses confirmed the spinel cubic structure and helped estimate average crystallite dimensions [7].

b) **Transmission electron microscopy (TEM):** TEM provided high-resolution imaging of the internal structure and morphology of the nanoparticles.

c) **Scanning electron microscopy (SEM):** SEM offered detailed surface imaging of the nanoparticles' morphology and topography.

d) **Energy-dispersive X-ray spectroscopy (EDX/EDS):** EDS (Energy-dispersive X-ray Spectroscopy) analyzed the elemental composition, revealing deviations in Co, Fe, and O content compared to theoretical values. These variations suggested oxidation state differences and synthesis-dependent stoichiometry.

e) **Raman Spectroscopy:** Raman spectroscopy was used to investigate molecular vibrations, confirming the structural integrity and cation distribution within the spinel lattice.

f) **The vibrating sample magnetometer:** Using a Vibrating Sample Magnetometer (VSM) (Cryogenics, Ioan Ursu Institute), the magnetic properties were measured under fields up to $12\,T$ across $4\,K - 300\,K$. Key magnetic parameters assessed include: Saturation Magnetization (M_s), Remanent Magnetization (M_r), Coercivity (H_c), Curie Temperature (T_c), Blocking Temperature (T_B) via $ZFC - FC$ protocol.

g) **Magnetic Nanoparticle Hyperthermia:** The hyperthermia potential of the particles was also evaluated, especially important for biomedical applications. High M_s and low H_c values are preferred for efficient heating under alternating magnetic fields

Chapter 4 Results

4.1 Characterization of $CoFe_2O_4$ core nanoparticles prepared via sol-gel and hydrothermal methods

This section it summarizes the comparison of $CoFe_2O_4$ nanoparticles made by sol-gel (SG) and hydrothermal ($Hydro$) methods, focusing on how synthesis affects structure, morphology, and magnetic behavior.

4.1.1 Structural and morphological characterization of $CoFe_2O_4$ cores nanoparticles

XRD Analysis (Figure 1, Figure 2 and Table 1) confirmed that both synthesis techniques produced a single-phase spinel with a well-defined cubic $Fd-3m$ crystal structure and high phase purity:

- Sol-gel: Crystallite size = $18.32 \pm 1.14\ nm$; lattice parameter = $0.838\ nm$
- Hydrothermal: Crystallite size = $13.77 \pm 1.13\ nm$; lattice parameter = $0.837\ nm$

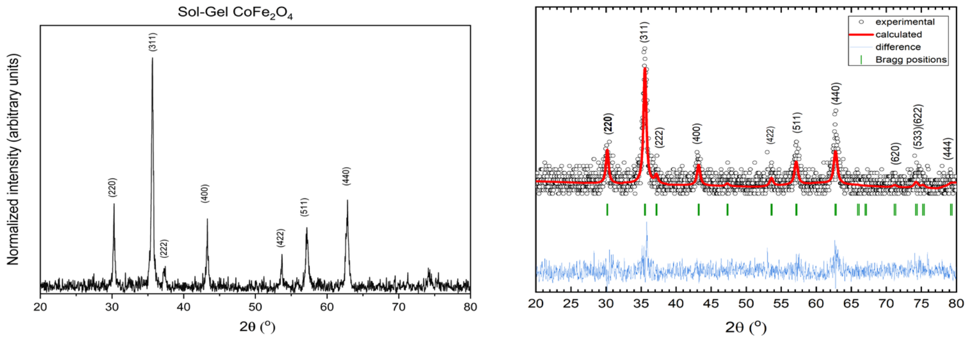

Figure 1: Left: XRD patterns of SG Core measured at room temperature; Right: Rietveld refinement results for SG Core.

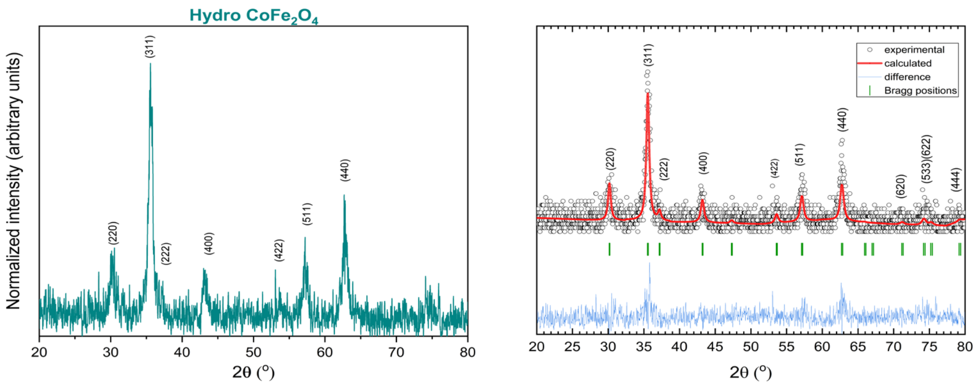

Figure 2: Left: XRD patterns of Hydro Core at room temperature; Right: Rietveld refinement results for Hydro Core.

Table 1: Summary of Mean Diameter D(nm) and Rietveld Refinement Parameters of SG and Hydro Core nanoparticles from Rietveld Refinement

	XRD Rietveld	XRD Rietveld	Rietveld Refinement Parameters					
	Cryst. diam. (D_R)(nm)	Lattice a_R(nm)	Rp	Rwp	Re	Chi2 (χ^2)	Bragg r factor	Rf factor
Sol-Gel Core	18.32 ± 1.14	0.838(5)	104	81.6	171.43	0.226	38.6	28.9
Hydro Core	13.77 ± 1.13	0.837(5)	120	84.2	169	0.249	33.9	19.7

TEM and SEM Morphology (Figures 3, 4, and 5): SG NPs have nearly spherical, aggregated clusters with an average TEM size of $35.8 \pm 8\,nm$ while Hydro NPs have nearly spherical too with more uniform average size $\sim 18.4 \pm 3\,nm$.

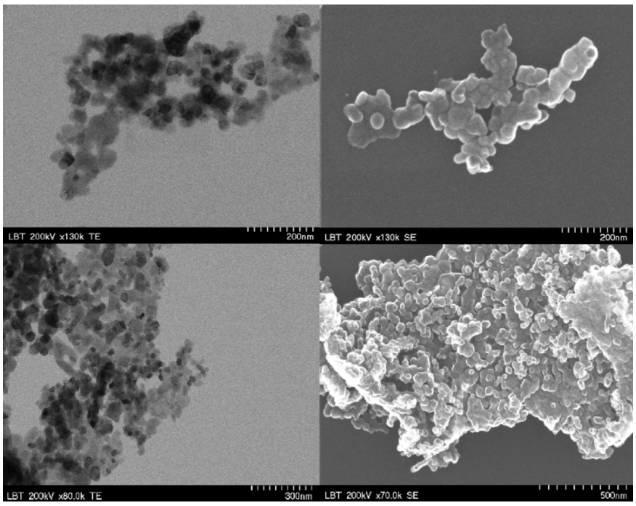

Figure 3: TEM (left) and SEM (right) images of the SG core at different magnifications

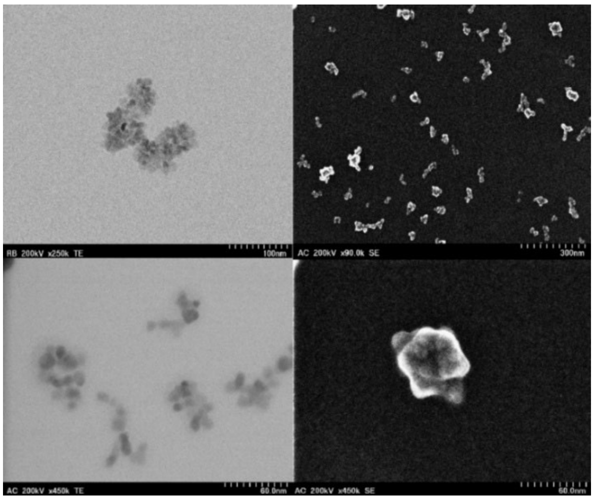

Figure 4: TEM (left) and SEM (right) images of the Hydro core at different magnifications.

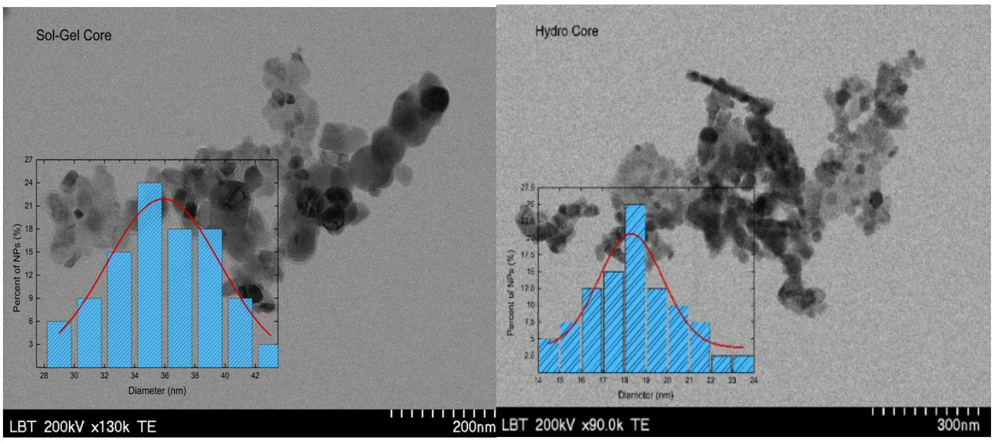

Figure 5: Size distribution histograms with TEM backgrounds for Sol-Gel (left) and Hydro (right) cores. The x-axis represents nanoparticle diameter, the y-axis shows percentage distribution, and the red curve indicates the fitted distribution.

EDS Composition Analysis (Table 2) reveals that both samples consistently contain the elements cobalt (Co), iron (Fe), and oxygen (O). The elemental distribution indicates a homogeneous composition throughout the samples, which supports the successful synthesis of the targeted material without detectable contamination or unwanted phases.

Table 2: Comparison of XRD (calculated and Rietveld refinement) and TEM results for the Sol-Gel and Hydro cores, along with theoretical and experimental atomic concentrations.

	Average Diameter D (nm)			Atomic concentration (Atoms %)					
	XRD D_c	XRD D_R	TEM	Co th.	Co ex.	Fe th.	Fe ex.	O th.	O ex.
Sol-Gel	23.049 ± 1.260	18.323 ± 1.140	35.8 ± 8	14.29	12.75	28.57	26.37	57.14	60.88
Hydro	16.415 ± 1.891	13.777 ± 1.131	18.4 ± 3	14.29	5.80	28.57	24.50	57.14	69.80

4.1.2 Magnetic characterization of $CoFe_2O_4$ nanoparticles

$CoFe_2O_4$ nanoparticles synthesized by sol-gel and hydrothermal methods were characterized magnetically at 300 K and 4 K under high magnetic fields. The related magnetic parameters were determined using the approach-to-saturation law.

- SG NPs: At room temperature, the magnetization increases gradually at low fields due to thermal fluctuations and approaches saturation at moderate fields. At low temperature reduced thermal agitation leads to a steeper magnetization rise and higher saturation magnetization. The hysteresis loops show soft magnetic behavior with low coercivity and moderate remanence at room temperature, while at low temperature, both coercivity and remanence increase, indicating enhanced magnetic ordering and anisotropy.

- Hydro NPs: Similar trends are observed, with a rapid magnetization increase at low fields at room temperature and saturation at moderate fields. At low temperature magnetization rises faster and saturation is reached at somewhat higher fields. The hysteresis loops exhibit narrow shapes indicative of soft magnetic materials, with low coercivity and remanence at room temperature and increased values at low temperature, reflecting stronger magnetic anisotropy and ordering.

Both synthesis methods yield nanoparticles with soft magnetic properties suitable for applications requiring low coercivity and efficient magnetization reversal. The sol-gel nanoparticles generally show higher saturation magnetization, especially at low temperatures. The increase of coercivity and remanence at 4 K for both samples reflects stronger magnetic anisotropy and ordering under reduced thermal energy conditions. These magnetic characteristics support the potential use of these nanoparticles in fields such as magnetic recording, biomedical treatments, and magnetic separation technologies.

All quantitative details and comparisons can be found summarized in Table 3.

Table 3: Summary of relevant magnetic parameters for the Sol-Gel and Hydro cores.

Core	Temperature (K)	Rising Curve Range (T)	Plateau Field (T)	M_s - Saturation Magnetization (emu/g)	M_r - Remanent Magnetization (emu/g)	H_c - Coercivity (T)
Sol-Gel	300	0-2	3	78.456 ± 0.057	22.25	0.06
	4	0-2	5-6	112.963 ± 0.240	61.78	0.348
Hydro.	300	0-2	3	76.509 ± 0.069	21.273	0.034
	4	0-3	5	80.260 ± 0.063	47.312	0.335

4.2 Characterization of $Co_{1-x}Zn_xFe_2O_4$ nanoparticles

$Co_{1-x}Zn_xFe_2O_4$ NPs were synthesized via the sol gel method with $x = 0, 0.05, 0.1, 0.2, \ldots, 1$, using sucrose and pectin serving as bio-derived poly-condensation and chelating agents.

4.2.1 Structural and morphological characterization of $Co_{1-x}Zn_xFe_2O_4$

XRD pattern analysis (Figure 6-a) confirms that all synthesized samples exhibit a single-phase cubic Fd-3m crystal structure. To accurately determine lattice parameters, Rietveld refinement was performed on all samples using FullProf software, with Figure 6-b showing a representative refinement for

$Co_{0.7}Zn_{0.3}Fe_2O_4$. The refinement results, summarized in Table 4, reveal a clear trend of increasing lattice parameters and unit cell volume with increasing Zn content, as illustrated in Figure 6-c. This trend aligns with theoretical expectations because Zn^{2+} ions, which preferentially occupy octahedral sites in the spinel lattice, have a larger ionic radius (0.74 Å in octahedral coordination) compared to Co^{2+} ions (0.65 Å), causing lattice expansion. In tetrahedral coordination, the ionic radius difference is smaller (0.60 Å for Zn^{2+} vs. 0.58 Å for Co^{2+}). The observed increase in lattice parameters is consistent with earlier studies over a limited composition range [10,11], but contrasts with findings in [12], where a decrease in lattice parameter was reported up to $x = 0.3$, followed by nonlinear increase at higher Zn content. Such discrepancies may result from differences in synthesis methods, thermal treatments, or sample purity. The sharp XRD peaks in our samples indicate high crystallinity, which may explain deviations from other reports influenced by defects or strain. Overall, the gradual lattice expansion confirms the successful incorporation of Zn into the spinel structure.

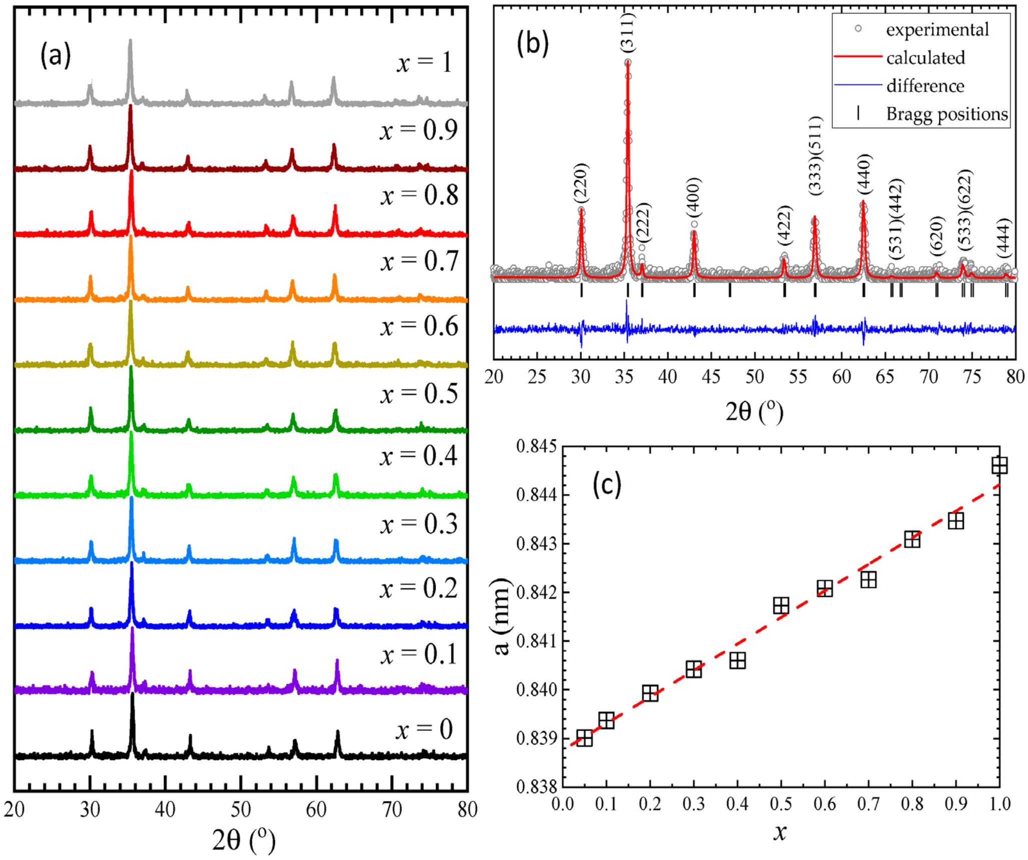

Figure 6: a) XRD patterns of $Co_{1-x}Zn_xFe_2O_4$ nanoparticles measured at room temperature, (b) Rietveld refinement analysis for $Co_{0.7}Zn_{0.3}Fe_2O_4$, (c) Variation of lattice parameter as a function of Zn concentration in $Co_{1-x}Zn_xFe_2O_4$ [13].

The crystallite sizes of $Co_{1-x}Zn_xFe_2O_4$ samples, calculated using the Debye–Scherrer formula after correcting for instrumental broadening, were found to be in the range of $30 - 40\ nm$ for all investigated compositions. These values indicate a consistent crystalline domain size across the series, suggesting that Zn substitution does not significantly disrupt the nanoscale structural coherence of the material.

TEM investigations provide further insights into the morphology and dispersion behavior of the NPs. The analysis reveals that the nanoparticles exhibit a strong tendency to agglomerate, driven primarily by intense magnetic interactions, which dominate over the significantly weaker electrostatic repulsion forces (Figure 7).

The TEM images reveal a wide size distribution, with individual NPs varying from $15\ nm$ to $70\ nm$, while the average particle diameter closely corresponds to the values derived from XRD analysis (Table 4). This correlation indicates that the majority of the nanoparticles are single crystals with high structural integrity and minimal lattice defects. However, the observed polydispersity suggests a non-uniform growth process, leading to variations in particle sizes. The error bars associated with TEM measurements indicate that the mean particle size obtained may be slightly larger than the mean diameter derived from XRD.

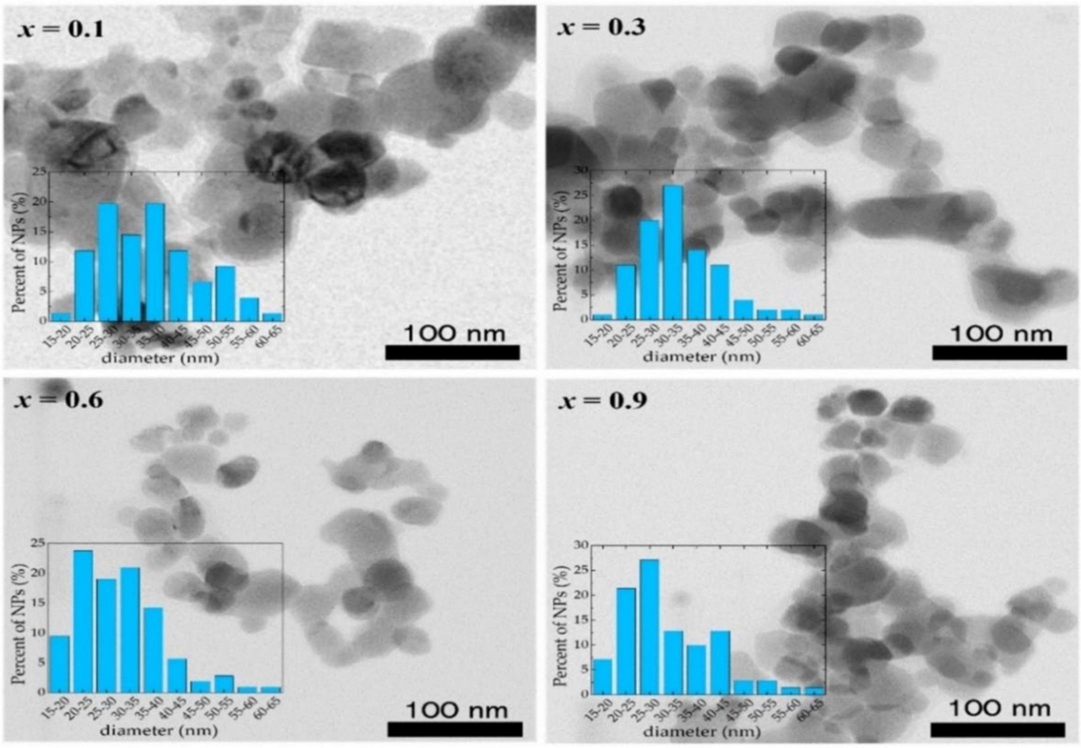

Figure 7: TEM images of $Co_{1-x}Zn_xFe_2O_4$ nanoparticles [13].

This variation arises from differences in measurement techniques: XRD primarily determines the coherently scattering domain size, whereas TEM provides the physical dimensions of entire nanoparticles, which may include structural agglomerates or surface modifications. As a result, these findings highlight the necessity of utilizing multiple characterization techniques to achieve a more thorough understanding of the structural and morphological properties of $Co_{1-x}Zn_xFe_2O_4$ NPs.

Table 4: Mean particle size of $Co_{1-x}Zn_xFe_2O_4$ nanoparticles, as determined from XRD and TEM analyses, along with the theoretical and experimental atomic composition obtained from EDS measurements [13].

Mean Diameter (nm)			Atomic Abundance (Atoms %)							
x	XRD	TEM	Co th.	Co ex.	Zn th.	Zn ex.	Fe th.	Fe ex.	O th.	O ex.
0.1	35 ± 2	38 ± 11	12.8	11.5	1.4	1.1	28.5	21.3	57.3	66.1
0.3	36 ± 2	35 ± 9	10.0	9.0	4.2	1.6	28.5	21.4	57.3	68.0
0.6	31 ± 1	31 ± 10	5.7	5.9	8.5	5.2	28.5	22.9	57.3	66.0
0.9	32 ± 1	31 ± 10	1.4	1.9	12.8	9.0	28.5	23.6	57.3	65.5

EDS analysis verified the presence of Co, Fe, Zn, and O in all examined samples, confirming the expected elemental composition with no significant impurities detected (Table 4).

Minor differences between theoretical and experimental atomic concentrations are within measurement uncertainty, confirming the high purity and structural integrity of $Co_{1-x}Zn_xFe_2O_4$ nanoparticles.

Raman spectroscopy provides detailed insight into cation distribution in spinel structures through analysis of vibrational modes. For spinels with $Fd-3m$ symmetry, five Raman-active modes (A_{1g}, E_g, and $3T_{2g}$) are expected [14–17]. These reflect atomic displacements and are sensitive to local environments.

Figure 8 shows Raman spectra for samples with $0.05 \leq x \leq 0.9$, featuring distinct peaks near $310, 350, 470, 560, 610, 650$ and $690\ cm^{-1}$. The $T_{2g}(1)$ mode ($\sim 180\ cm^{-1}$) lies between those of magnetite and Mn-Zn-doped ferrites [18–22]. Peak positions and intensities vary with Zn content, indicating cationic effects. In $CoFe_2O_4$, A_{1g} peaks at ~ 620 and $\sim 695\ \ cm^{-1}$ relate to Co/Fe vibrations at tetrahedral sites, while $T_{2g}(3)$ modes at ~ 470 and $\sim 575\ cm^{-1}$ reflect octahedral coordination [21]. For $ZnFe_2O_4$, overlapping A_{1g} features at 641 and $685\ cm^{-1}$ arise from ZnO_4 and FeO_4 units, $T_{2g}(3)$ modes appear at ~ 470 and $\sim 510\ cm^{-1}$.

Spectral deconvolution identified A_{1g} components: $605-610\ cm^{-1}$ ($Co-O$), $635-650\ cm^{-1}$ ($Zn-O$), and $680-690\ cm^{-1}$ ($Fe-O$). Six-mode fits from 380–800 cm^{-1} ($FWHM$ $40-70\ cm^{-1}$) showed only minor peak shifts ($\pm\ 10\ cm^{-1}$), confirming cobalt ferrite phase retention (Table 5) [23].

Figure 9 shows that at low Zn content, Zn^{2+} mainly substitutes Co^{2+} in tetrahedral sites, reducing the $610\ cm^{-1}$ $Co-O$ peak. At $x > 0.4$, Zn occupancy in octahedral sites rises, enhancing the $510\ cm^{-1}$ $Zn-O$ peak. Concurrent shifts in Fe related peaks at ~ 680 and $\sim 470\ cm^{-1}$ reflect inversion degree changes and cation redistribution.

These results confirm Raman spectroscopy as an effective method for mapping site-specific substitutions in ferrites [13].

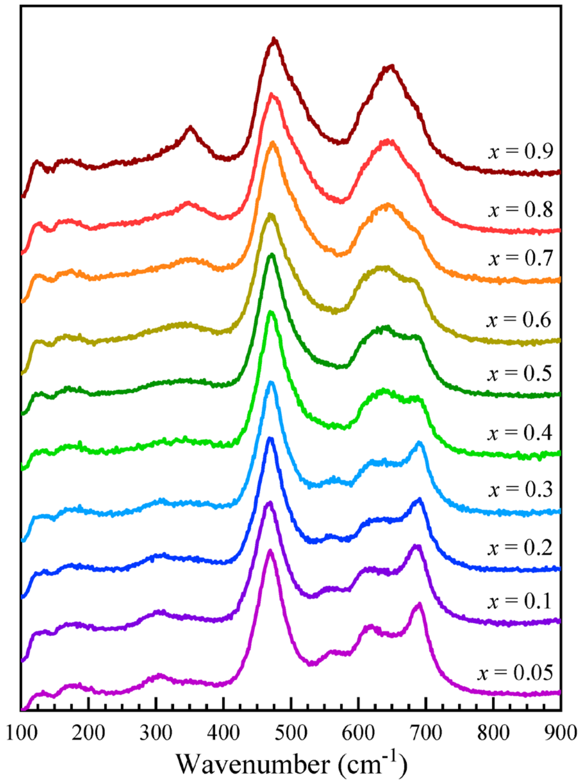

Figure 8: Raman spectra of $Co_{1-x}Zn_xFe_2O_4$ nanoparticles [13].

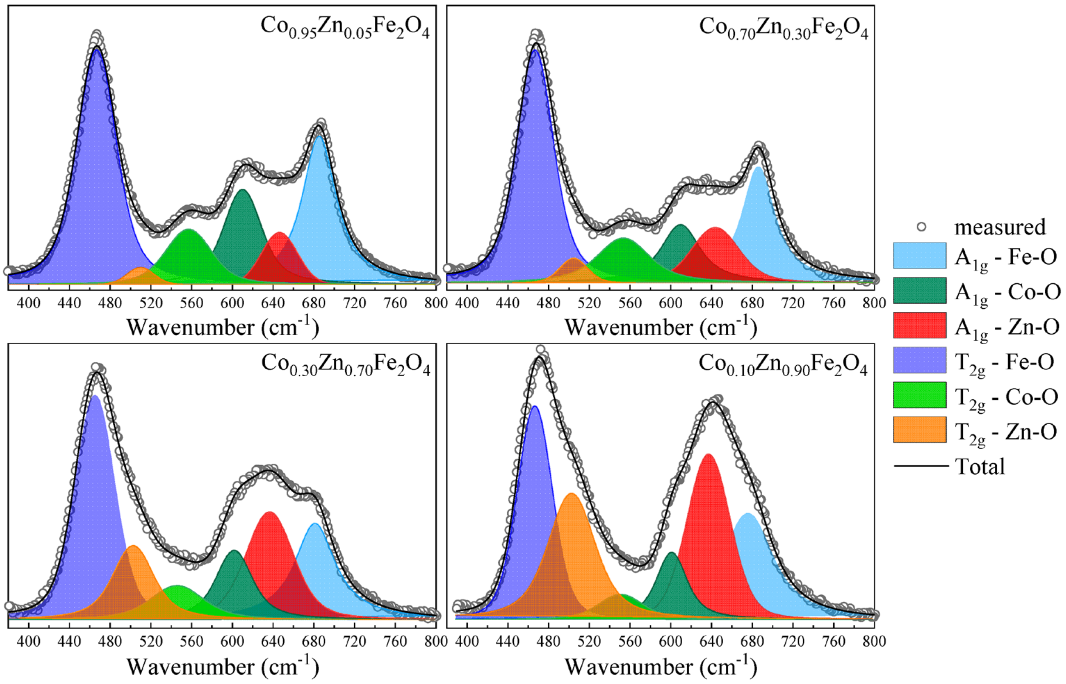

Figure 9: Fitting results for Raman spectra of $Co_{1-x}Zn_xFe_2O_4$ nanoparticles [13].

4.2.2 Magnetic characterization of $Co_{1-x}Zn_xFe_2O_4$

Magnetic measurements at $4\ K$ under fields up to $10\ T$ (Figure 10), analyzed using the approach-to-saturation law, revealed that the saturation magnetization of $Co_{1-x}Zn_xFe_2O_4$ nanoparticles increase with Zn content up to $x = 0.5$, then sharply decreases at higher concentrations (Figure 11). This differs from earlier reports where the maximum was observed at $x = 0.2$ [24] or $x = 0.4$ [11,25]. The higher M_s peak found at $x = 0.5$ in this study likely results from the high crystallinity and structural quality of the samples.

The initial increase in M_s is attributed to the preferential substitution of Co^{2+} by nonmagnetic Zn^{2+} in tetrahedral sites, weakening antiferromagnetic $A - B$ interactions and enhancing net magnetization. This interpretation is supported by Raman spectroscopy, which confirms Zn occupancy at tetrahedral sites for $x < 0.5$. Beyond $x \geq 0.5$, M_s declines due to Zn replacing Co^{2+} in octahedral sites, disrupting magnetic coupling. The nonlinear M_s behavior reflects changes in the inversion degree with Zn substitution.

Room-temperature hysteresis loops (Figure 12) show that coercivity peaks at $x = 0.1$, then decreases with higher Zn content. At $300\ K$ under $4\ T$ (Figure 13), magnetization trends resemble those observed at $4\ K$, reinforcing the correlation between magnetic behavior at low and room temperatures.

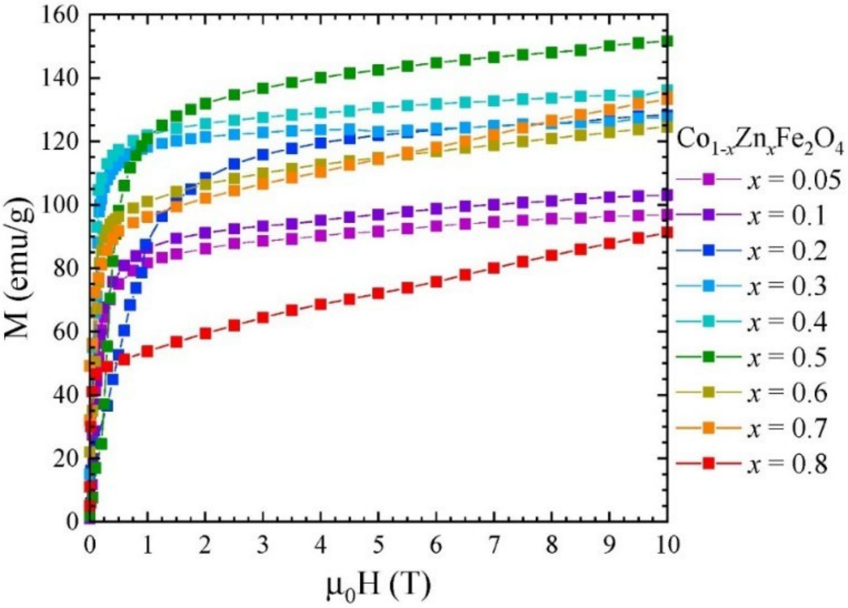

Figure 10: Magnetization isotherms of $Co_{1-x}Zn_xFe_2O_4$ nanoparticles measured at 4 K [13].

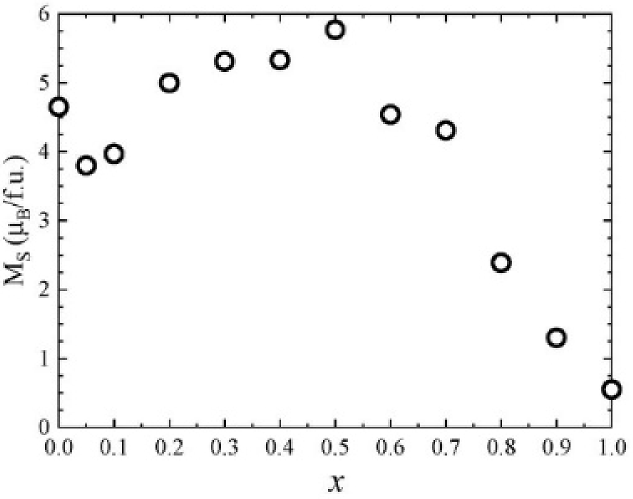

Figure 11: Saturation magnetization of $Co_{1-x}Zn_xFe_2O_4$ *nanoparticles at 4 K* [13] .

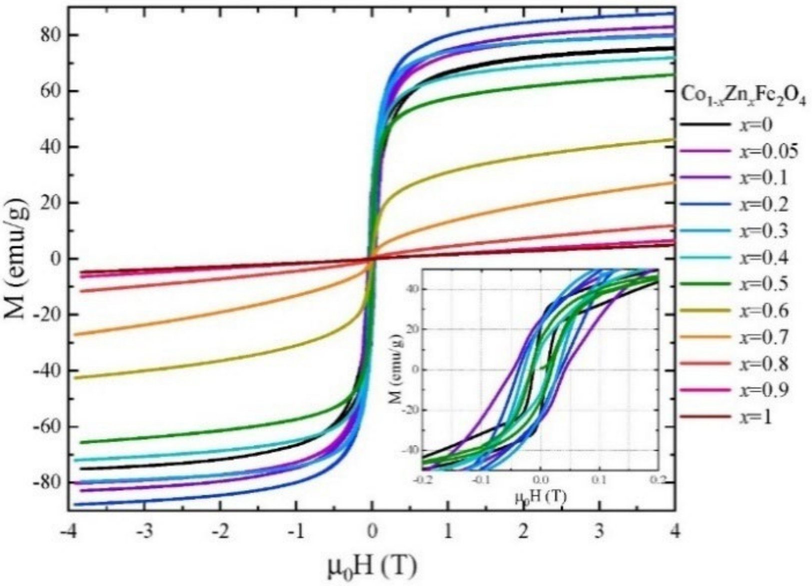

Figure 12: Hysteresis loops measured at room temperature for $Co_{1-x}Zn_xFe_2O_4$ *nanoparticles* [13].

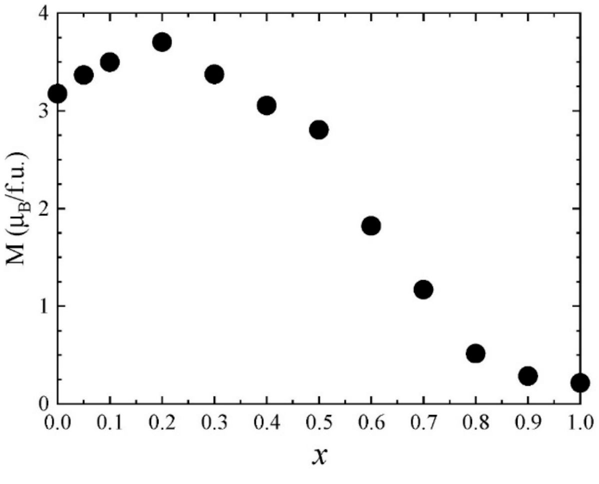

Figure 13: Magnetization measurements at 4 T for $Co_{1-x}Zn_xFe_2O_4$ *nanoparticles at 300 K* [13].

The heating efficiency of selected $Co_{1-x}Zn_xFe_2O_4$ samples dispersed in water ($1\,mg_{MNPs}/mL$) was evaluated under alternating magnetic fields ($10-60\,kA/m$, $355\,kHz$), and SAR values were calculated using Box–Lucas fitting (Figure 14). Pure $CoFe_2O_4$ ($x=0$) showed low SAR values, consistent with prior studies [26–28]. Zn doping at 5% and 10% caused minimal improvement, with noticeable enhancement only at higher field strengths. A significant SAR increase was observed for 20% Zn doped samples, especially at moderate fields, suggesting improved heating performance. At 30% Zn, despite reduced M_s and H_c, SAR values rose sharply with field amplitude, showing up to threefold increase compared to lower Zn content. This linear SAR growth (up to 840 W/g_{MNPs}) reflects non-saturating magnetization behavior, aligning with trends reported in and confirming high potential for magnetic hyperthermia applications [28,29].

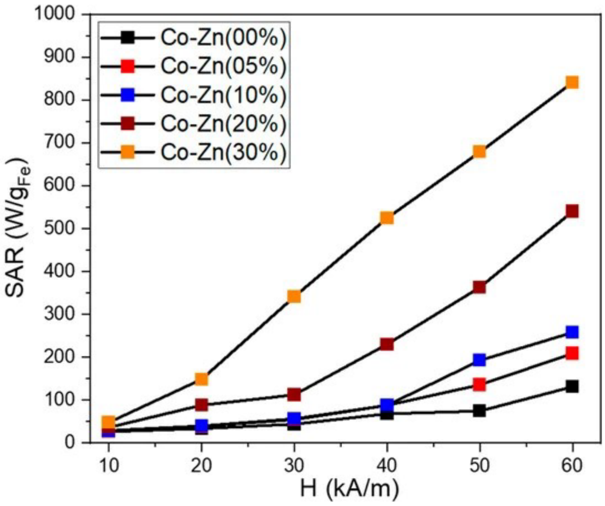

Figure 14: Specific absorption rate (SAR) as a function of magnetic field amplitude (H) for five ferrite samples dispersed in water at a concentration of 1 mg$_{MNPs}$/mL [13].

4.3 Characterization of $Co_{1-x}Mn_xFe_2O_4$ nanoparticles

In our study $Co_{1-x}Mn_xFe_2O_4$ NPs were synthesized via the hydrothermal method using Iron (III) acetylacetonate, Cobalt (II) acetylacetonate, and Manganese (II) acetylacetonate as precursor materials.

4.3.1 Structural and Morphologic characterization of $Co_{1-x}Mn_xFe_2O_4$

XRD analysis (Figure 15) confirms that all $Co_{1-x}Mn_xFe_2O_4$ samples possess a single-phase cubic $Fd-3m$ structure with no detectable impurities, indicating high purity. Rietveld refinement shows a nearly linear increase in lattice parameters with rising Mn content, following Vegard's law, due to the larger ionic radius of Mn^{2+} compared to Co^{2+} (Figure 16). Selected refinement results for $x=0.3$ and $x=0.8$ (Figure 15-b, c) support these findings. The trend is consistent with previous reports on narrower composition ranges [30–32].

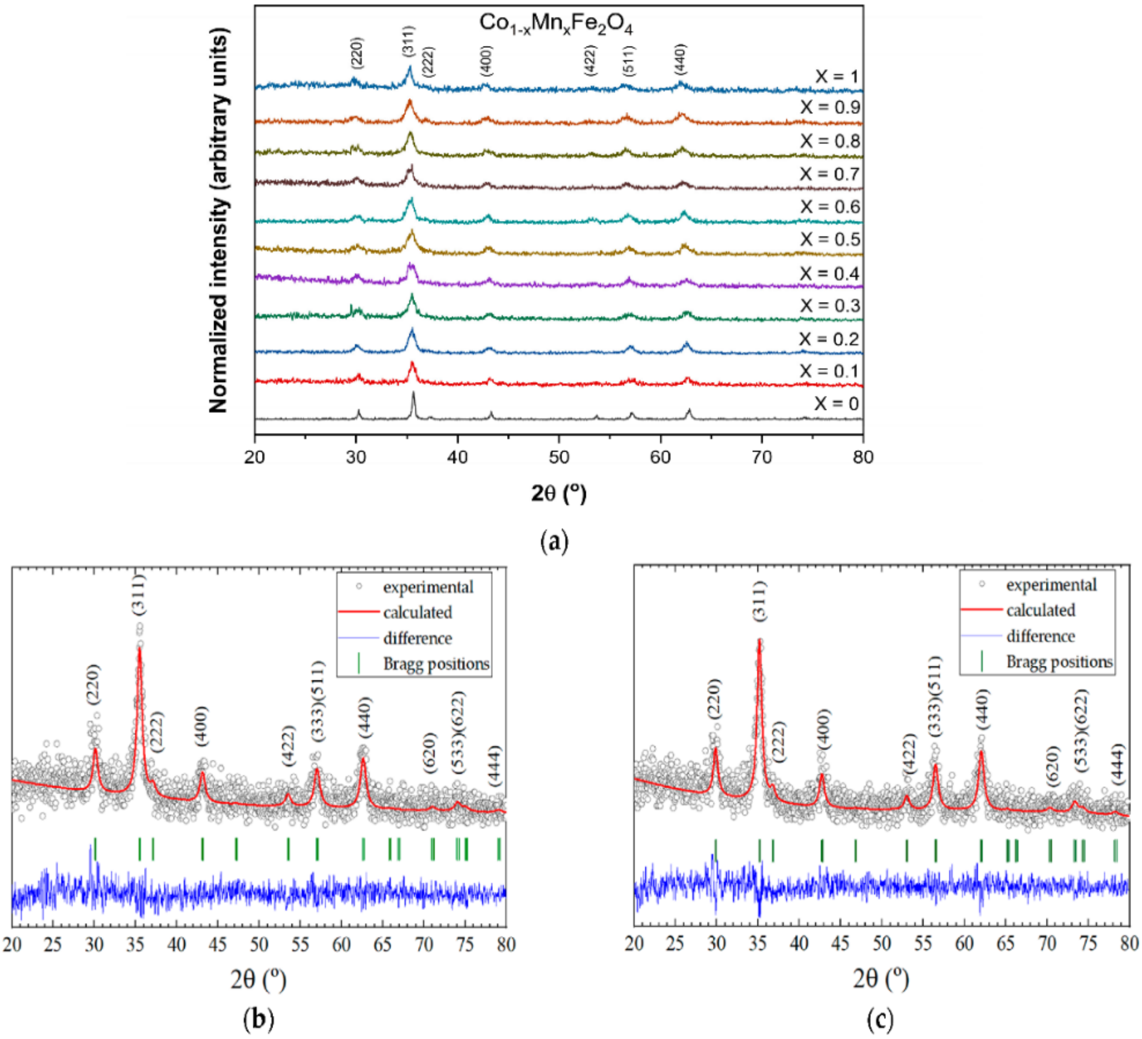

Figure 15: (a) XRD patterns of $Co_{1-x}Mn_xFe_2O_4$ nanoparticles at room temperature; Rietveld refinement results for samples with x = 0.3 (b) and x = 0.8 (c)[33].

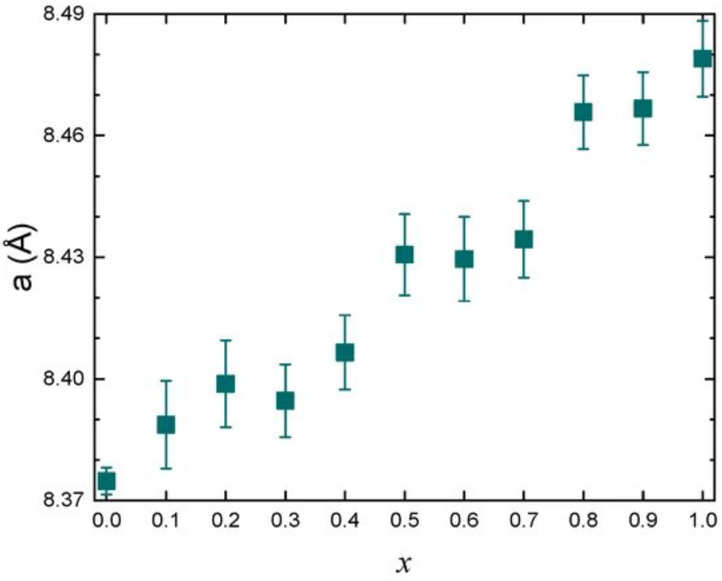

Figure 16: Variation of lattice parameters with Mn content in $Co_{1-x}Mn_xFe_2O_4$ nanoparticles [33].

A thorough examination of the TEM images reveals that the NPs have sizes ranging from 7 nm to 15 nm, with an average diameter that closely corresponds to the values obtained from XRD measurements (Figure 17).

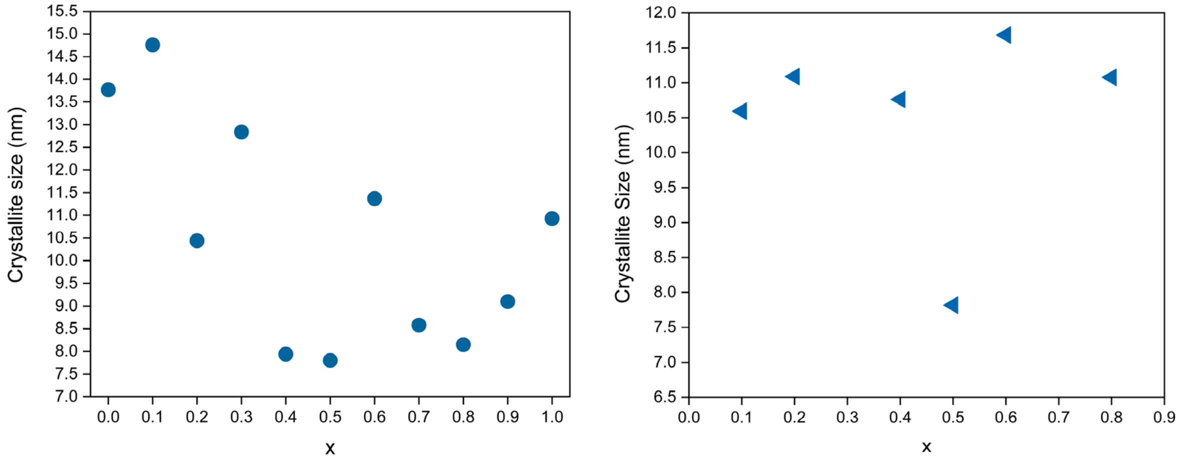

Figure 17: Composition-dependent variation of crystallite sizes determined from XRD (left) and TEM (right)[33].

This consistency suggests that the majority of $Co_{1-x}Mn_xFe_2O_4$ nanoparticles exist as single crystals with high crystallinity, exhibiting minimal structural defects. The composition-dependent variation in NPs size, as determined from TEM measurements, is shown in Figure 18 and follows a trend similar to that observed in XRD-based size calculations.

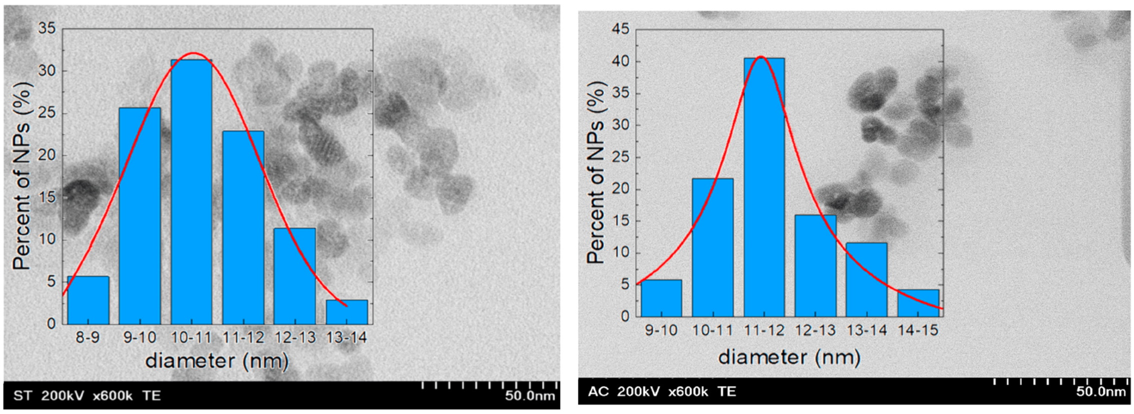

Figure 18: TEM images of $Co_{1-x}Mn_xFe_2O_4$ nanoparticles along with size distributions for the samples with x=0.1 (left) and x=0.6, (right) [33].

To further analyze the composition of the synthesized nanoparticles, EDS elemental analysis was conducted. The results confirmed the presence of Co, Fe, Mn, and O in all examined samples. As an example, Figure 19-a, b presents the TEM image and corresponding EDS spectra for the $Co_{0.8}Mn_{0.2}Fe_2O_4$ NPs and Figure 20 confirming their expected elemental composition.

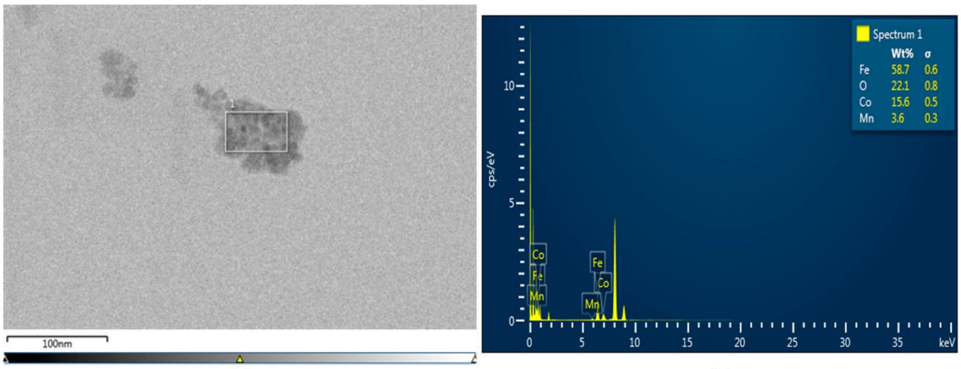

(a) (b)

Figure 19: TEM image (a) and EDS spectrum (b) of $Co_{0.8}Mn_{0.2}Fe_2O_4$ nanoparticles, confirming elemental composition and Mn incorporation [33].

Additionally, the EDS spectra demonstrated the absence of detectable impurities, reinforcing the high purity of the synthesized materials. Furthermore, elemental mapping for the $x = 0.2$ sample, illustrating the homogeneous spatial distribution of Co, Mn, Fe, and O across the analyzed region.

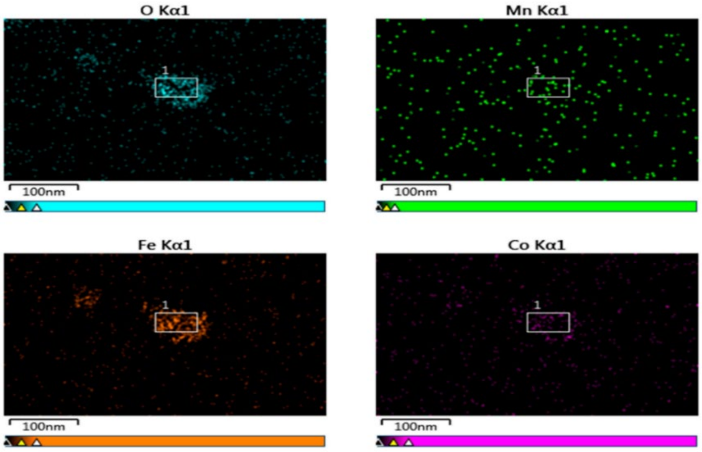

Figure 20: Elemental mapping of $Co_{0.8}Mn_{0.2}Fe_2O_4$ nanoparticles, showing uniform distribution of Co, Mn, and Fe [33].

Raman analysis (Figures 21, 22) confirms the cubic $Fd-3m$ symmetry and reveals five characteristic vibrational modes consistent with spinel ferrites. The spectra show increasing complexity with Mn substitution, as expected from group theory and previous studies. Distinct $Co-O/Mn-O$ and $Fe-O$ bands, along with overlapping $Mn-O/Fe-O$ modes, reflect cation distribution across tetrahedral and octahedral sites [13,19,34].

As Mn content increases, the tetrahedral $Co-O/Mn-O$ band ($\sim 600\ cm^{-1}$) gains intensity relative to the $Fe-O$ band ($\sim 677\ cm^{-1}$), and the $T_{2g}(2)$ band shifts from ~466 to 445 cm^{-1} (Figures 50-c, d). These trends indicate increased Mn incorporation into both lattice sites. Though the intensity ratio of A_{1g} modes suggest site occupancy changes, it cannot precisely resolve Mn location due to mode overlap. Nonetheless, the consistent $Fe-O$ signal confirms the presence of Fe^{3+} in tetrahedral sites across all compositions.

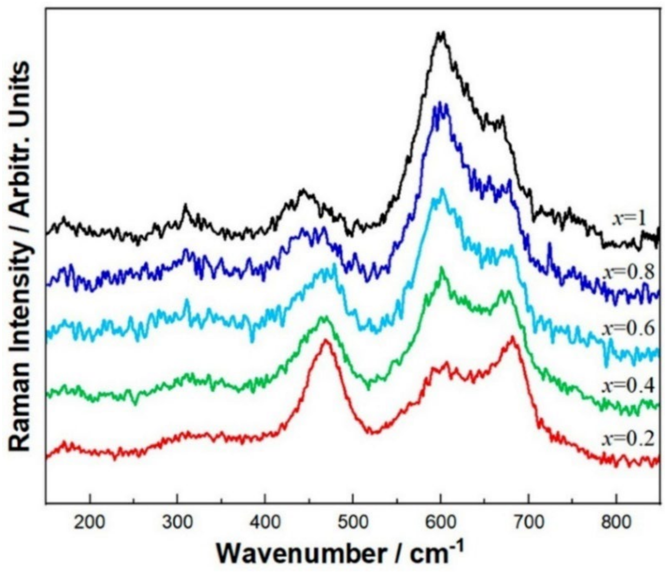

Figure 21: Raman spectra of selected $Co_{1-x}Mn_xFe_2O_4$ ferrites [33].

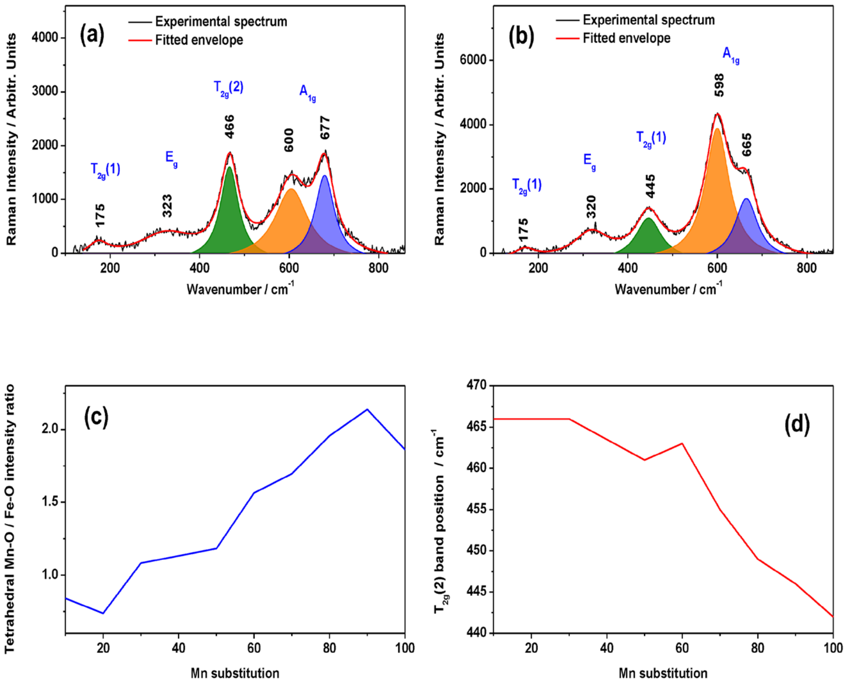

Figure 22: Raman spectra and deconvoluted main bands of Mn-substituted ferrites for substitution levels of $x = 0.2$ (a) and $x = 0.9$ (b). Panels (c) and (d) show, respectively, the variation of the intensity ratio between the 600 and 677 cm^{-1} modes (indicative of tetrahedral Mn–O/Fe–O) and the shift in the $T_2g(2)$ band position as a function of Mn content [33].

4.3.2 Magnetic characterization of $Co_{1-x}Mn_xFe_2O_4$

Magnetization measurements under high magnetic fields revealed that saturation is achieved up to $x \approx 0.7$, but not for $x = 1$ even at $12\ T$ (Figure 23). The saturation magnetization values at $4.2\ K$, calculated using the approach-to-saturation law and summarized in Table 5, are higher than previously reported likely due to improved crystallinity and optimized cation distribution. Theoretical magnetic moments, based on Raman-verified cation distributions and ion spin values, agree closely with experimental values, confirming the influence of site occupancy, particularly Mn^{4+} in tetrahedral sites [32,35–37].

The hysteresis loops of nanoparticles, measured at $4.2\ K$ and $300\ K$ (Figure 24), show clear magnetic behavior at low temperature but are nearly closed at room temperature due to thermal effects and small particle size. At $4.2\ K$, coercivity decreases with increasing Mn content ($x > 0.2$), reaching near-zero at $x = 1$. The remanent magnetization peaks around $x \approx 0.7$ before declining (Figure 25). At $300\ K$, both coercivity and remanence are negligible for all samples.

$ZFC - FC$ curves measured under $0.05\ T$ (Figure 26) show decreasing blocking temperatures with increasing Mn content, in agreement with previous findings suggesting spin-glass-like behavior and superparamagnetic relaxation in smaller particles [38–40].

The squareness ratio (M_r/M_s) remains below 0.5 at room temperature, indicating single-domain behavior and predominant magnetostatic interactions. These magnetic characteristics, combined with high saturation magnetization and tunable coercivity, support the potential use of these NPs in magnetoelectric core–shell structures, such as $Co_{1-x}Mn_xFe_2O_4@BaTiO_3$, for biomedical applications like cancer-specific electroporation. Additional potential uses include magnetic microemulsions and hydrogels, demonstrating their versatility in advanced therapeutic technologies [41–44].

Table 5: Site Occupancies of Cations and Saturation Magnetization for $Co_{1-x}Mn_xFe_2O_4$ Samples at 4.2 K and 300 K [33].

x	**Cation Distribution**		**M_S (µB) Calc.**	**M_S (µB) Exp. T = 4.2 K**	**M_S (µB) Exp. T = 300 K**
	(Tetrahedral Site)	**(Octahedral Sites)**			
0	$(Co_{0.08}Fe_{0.92})$	$(Co_{0.92}Fe_{1.08})$	3.32	3.38	3.20
0.1	$(Co_{0.4}Mn_{0.1}Fe_{0.5})$	$(Co_{0.5}Fe_{1.5})$	5.20	5.16	4.05
0.2	$(Co_{0.2}Mn_{0.2}Fe_{0.6})$	$(Co_{0.6}Fe_{1.4})$	5.00	4.86	3.75
0.3	$(Co_{0.1}Mn_{0.3}Fe_{0.6})$	$(Co_{0.6}Fe_{1.4})$	5.20	5.12	3.30
0.4	$(Co_{0.3}Mn_{0.3}Fe_{0.4})$	$(Co_{0.3}Mn_{0.1}Fe_{1.6})$	5.80	5.81	4.05
0.5	$(Mn_{0.4}Fe_{0.6})$	$(Co_{0.5}Mn_{0.1}Fe_{1.4})$	4.00	3.71	2.60
0.6	$(Mn_{0.15}Fe_{0.85})$	$(Co_{0.4}Mn_{0.45}Fe_{1.5})$	4.80	4.78	3.45
0.7	$(Co_{0.3}Mn_{0.6}Fe_{0.1})$	$(Co_{0.1}Fe_{1.9})$	5.80	5.86	4.10
0.8	$(Co_{0.2}Mn_{0.7}Fe_{0.1})$	$(Mn_{0.1}Fe_{1.9})$	5.60	5.48	3.75
0.9	$(Co_{0.1}Mn_{0.7}Fe_{0.3})$	$(Mn_{0.3}Fe_{1.7})$	5.80	5.55	3.80
1.0	$(Mn_{0.33}Fe_{0.67})$	$(Mn_{0.67}Fe_{1.33})$	6.33	6.78	4.60

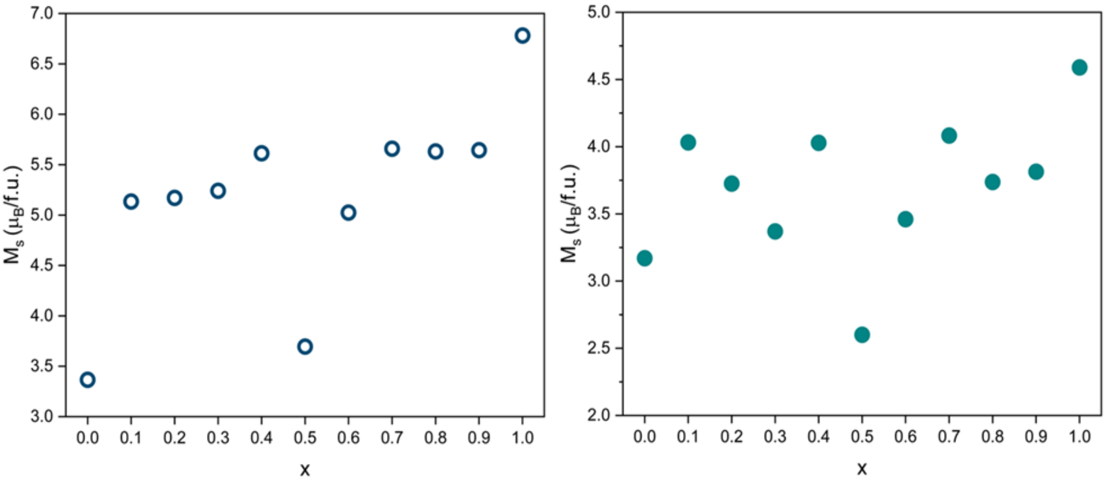

Figure 23: Ms of $Co_{1-x}Mn_xFe_2O_4$ nanoparticles at 4.2 K (left) and 300 K (right), showing the effect of Mn concentration (x).

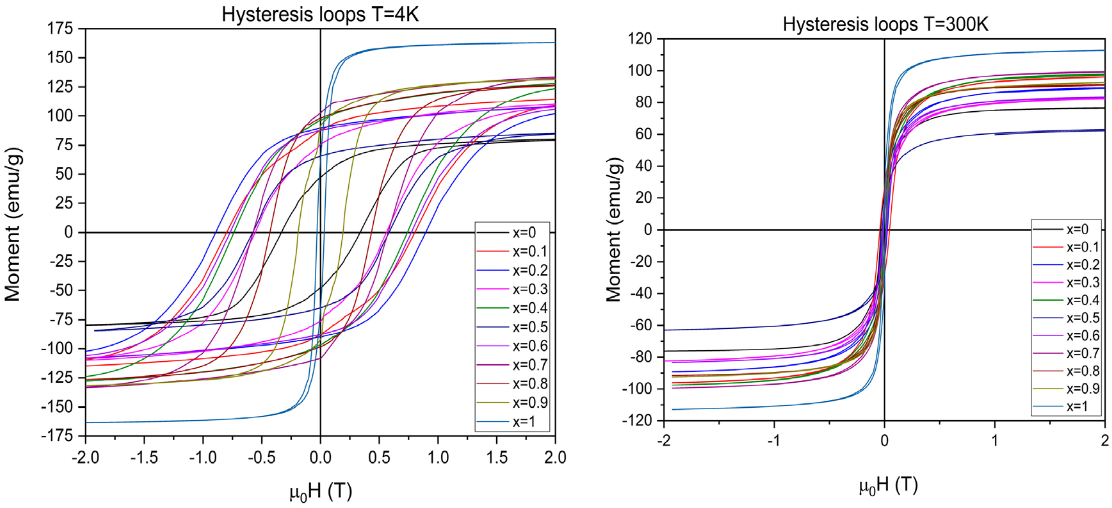

Figure 24: Hysteresis loops for $Co_{1-x}Mn_xFe_2O_4$ nanoparticles at 4.2 K (left) and 300 K (right) [33].

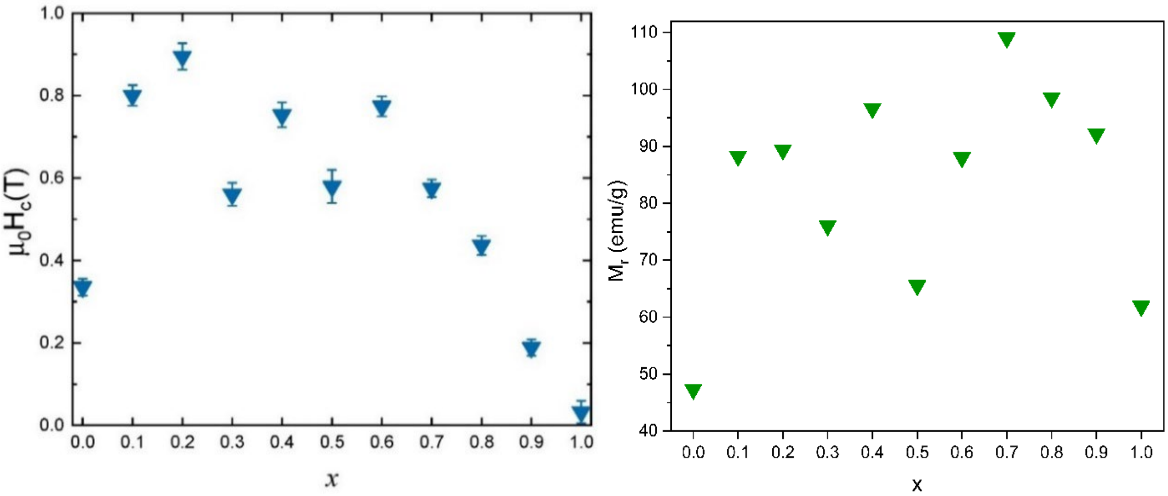

Figure 25: The variation of coercive field and remanent magnetization as a function of manganese content (x) at 4.2 K [33].

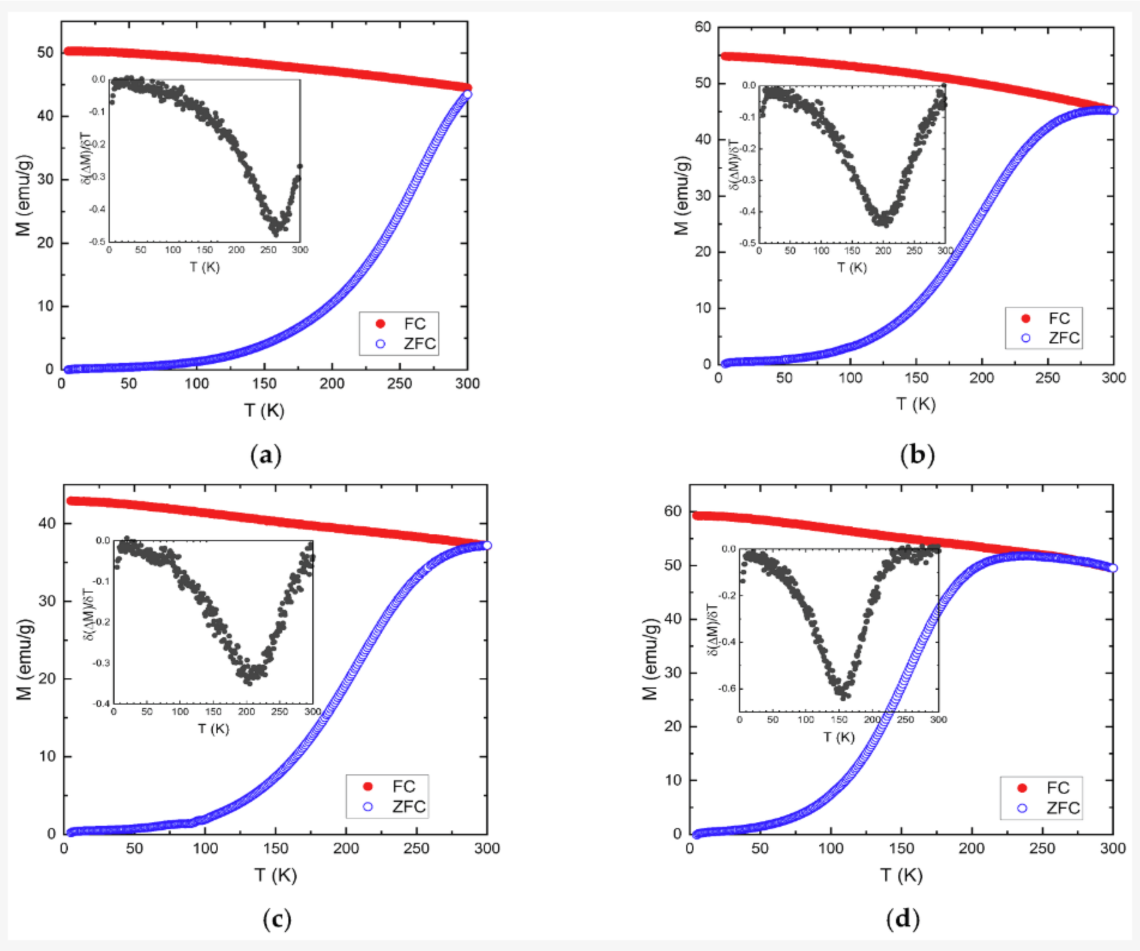

Figure 26: The temperature dependences of magnetization measured in the ZFC and FC regimes for samples with $x = 0.2$, $x = 0.4$, $x = 0.6$, and $x = 0.8$ are presented [33].

Conclusions

This dissertation investigates the synthesis, structure, and magnetic behavior of $CoFe_2O_4$ nanoparticles and their Zn and Mn substituted variants for biomedical and technological applications. Nanoparticles were synthesized using sol-gel and hydrothermal methods and characterized via XRD, TEM, Raman, and VSM. XRD confirmed spinel cubic structures in all samples.

Zn substitution preserved the spinel structure and increased particle size. Raman spectra revealed structural distortions and cation redistribution. Saturation magnetization peaked at $x = 0.5$ ($\sim 150\ emu/g$), while coercivity decreased after $x > 0.1$. Zn-substituted $CoFe_2O_4$ nanoparticles are particularly useful for magnetic hyperthermia applications in biomedicine due to their enhanced specific absorption rate (SAR) values.

Mn substitution also maintained spinel structure, with lattice expansion and Raman shifts confirming Mn incorporation. Saturation magnetization showed a non-linear trend, peaking at $x = 1$ ($\sim 165\ emu/g$ at $4\ K$), while coercivity and remanence increased with doping. $ZFC - FC$ data confirmed single-domain behavior and blocking temperatures below room temperature. These nanoparticles are valuable for tuning magnetic properties across a wide range, making them suitable for both technological and biomedical applications.

References

[1] Khalid M, Younas M, Ashiq M, Boukhris I, Kebaili I, Dildar M, et al. Magneto-electric coupled CoFe2O4/MWCNTs nanocomposites for energy storage applications. J Solgel Sci Technol n.d. https://doi.org/10.1007/s10971-024-06613-4.

[2] Mombini K, Gheisari K, Reihanian M. Exploring novel magnetic behaviors in cobalt-doped magnetite synthesized by plasma arc discharge method. Mater Today Commun 2024;41:110550. https://doi.org/10.1016/J.MTCOMM.2024.110550.

[3] Muhammad A, Sato-Turtelli R, Kriegisch M, Grössinger R, Kubel F, Konegger T. Large enhancement of magnetostriction due to compaction hydrostatic pressure and magnetic annealing in CoFe 2O 4. J Appl Phys 2012;111. https://doi.org/10.1063/1.3675489.

[4] Köseoğlu Y, Alan F, Tan M, Yilgin R, Öztürk M. Low temperature hydrothermal synthesis and characterization of Mn doped cobalt ferrite nanoparticles. Ceram Int 2012;38:3625–34. https://doi.org/10.1016/j.ceramint.2012.01.001.

[5] Nlebedim IC, Snyder JE, Moses AJ, Jiles DC. Dependence of the magnetic and magnetoelastic properties of cobalt ferrite on processing parameters. J Magn Magn Mater 2010;322:3938–42. https://doi.org/10.1016/j.jmmm.2010.08.026.

[6] Néel ML. Propriétés magnétiques des ferrites ; ferrimagnétisme et antiferromagnétisme. Ann Phys 1948;12:137–98.

[7] Kittel C, Holcomb DF. Introduction to Solid State Physics. Am J Phys 1967;35:547–8. https://doi.org/10.1119/1.1974177.

[8] Hench LL, West JK. The Sol-Gel Process. vol. 90. 1990.

[9] Yoshimura M, Byrappa AK. Hydrothermal processing of materials: past, present and future n.d. https://doi.org/10.1007/s10853-007-1853-x.

[10] Hermosa GC, Liao C-S, Wu H-S, Wang S-F, Liu T-Y, Jeng K-S, et al. Green Synthesis of Magnetic Ferrites (Fe3O4, CoFe2O4, and NiFe2O4) Stabilized by Aloe Vera Extract for Cancer Hyperthermia Activities. IEEE Trans Magn 2022;58:1–7. https://doi.org/10.1109/TMAG.2022.3158835.

[11] Atif M, Asghar MW, Nadeem M, Khalid W, Ali Z, Badshah S. Synthesis and investigation of structural, magnetic and dielectric properties of zinc substituted cobalt ferrites. Journal of Physics and Chemistry of Solids 2018;123:36–42. https://doi.org/10.1016/J.JPCS.2018.07.010.

[12] Li W, Fa-Shen L. Structural and magnetic properties of Co 1- *x* Zn *x* Fe 2 O 4 nanoparticles. Chinese Physics B 2008;17:1858–62. https://doi.org/10.1088/1674-1056/17/5/052.

[13] Szatmari A, Bortnic R, Souca G, Hirian R, Barbu-Tudoran L, Nekvapil F, et al. The Influence of Zn Substitution on Physical Properties of CoFe2O4 Nanoparticles 2022. https://doi.org/10.3390/nano13010189.

[14] G. A. de Wijs, C. M. Fang, G. Kresse, G. de With. First-principles calculation of the phonon spectrum of MgAl2O4 spinel. Phys Rev B 2002;65:94305. https://doi.org/10.1103/PhysRevB.65.094305.

[15] Lazzeri M, Thibaudeau P. Ab initio Raman spectrum of the normal and disordered MgAl2O4. Phys Rev B 2006;74:140301. https://doi.org/10.1103/PhysRevB.74.140301.

[16] Graves PR, Johnston C, Campaniello JJ. Raman scattering in spinel structure ferrites. Mater Res Bull 1988;23:1651–60. https://doi.org/10.1016/0025-5408(88)90255-3.

[17] Wang Z, Lazor P, Saxena SK, O'Neill HSC. High pressure Raman spectroscopy of ferrite MgFe2O4. Mater Res Bull 2002;37:1589–602. https://doi.org/10.1016/S0025-5408(02)00819-X.

[18] Testa-Anta M, Ramos-Docampo MA, Comesaña-Hermo M, Rivas-Murias B, Salgueiriño V. Raman spectroscopy to unravel the magnetic properties of iron oxide nanocrystals for bio-related applications. Nanoscale Adv 2019;1:2086–103. https://doi.org/10.1039/C9NA00064J.

[19] Nekvapil F, Bunge A, Radu T, Cinta Pinzaru S, Turcu R. Raman spectra tell us so much more: Raman features and saturation magnetization for efficient analysis of manganese zinc ferrite nanoparticles. Journal of Raman Spectroscopy 2020;51:959–68. https://doi.org/https://doi.org/10.1002/jrs.5852.

[20] Nekvapil F, Bortnic R-A, Leoştean C, Barbu-Tudoran L, Bunge A. Characterization of the Lattice Transitions and Impurities in Manganese and Zinc Doped Ferrite Nanoparticles by Raman Spectroscopy and X-ray Diffraction (XRD). Anal Lett 2022;56:42–52. https://doi.org/10.1080/00032719.2022.2083145.

[21] Thota S, Kashyap SC, Sharma SK, Reddy VR. Micro Raman, Mossbauer and magnetic studies of manganese substituted zinc ferrite nanoparticles: Role of Mn. Journal of Physics and Chemistry of Solids 2016;91:136–44. https://doi.org/10.1016/J.JPCS.2015.12.013.

[22] Chandramohan P, Srinivasan MP, Velmurugan S, Narasimhan S V. Cation distribution and particle size effect on Raman spectrum of CoFe2O4. J Solid State Chem 2011;184:89–96. https://doi.org/10.1016/J.JSSC.2010.10.019.

[23] Galinetto P, Albini B, Bini M, Cristina Mozzati M. Raman spectroscopy in Zinc Ferrites Nanoparticles. In: do Nascimento GM, editor. Raman Spectroscopy, Rijeka: IntechOpen; 2018. https://doi.org/10.5772/intechopen.72864.

[24] Slatineanu T, Iordan AR, Oancea V, Palamaru MN, Dumitru I, Constantin CP, et al. Magnetic and dielectric properties of Co–Zn ferrite. Materials Science and Engineering: B 2013;178:1040–7. https://doi.org/10.1016/J.MSEB.2013.06.014.

[25] Li W, Fa-Shen L. Structural and magnetic properties of Co 1- *x* Zn *x* Fe 2 O 4 nanoparticles. Chinese Physics B 2008;17:1858–62. https://doi.org/10.1088/1674-1056/17/5/052.

[26] Sathya A, Guardia P, Brescia R, Silvestri N, Pugliese G, Nitti S, et al. CoxFe3–xO4 Nanocubes for Theranostic Applications: Effect of Cobalt Content and Particle Size. Chemistry of Materials 2016;28:1769–80. https://doi.org/10.1021/acs.chemmater.5b04780.

[27] Mameli V, Musinu A, Ardu A, Ennas G, Peddis D, Niznansky D, et al. Studying the effect of Zn-substitution on the magnetic and hyperthermic properties of cobalt ferrite nanoparticles † 2016;8:10124. https://doi.org/10.1039/c6nr01303a.

[28] Iacovita C, Stiufiuc GF, Dudric R, Vedeanu N, Tetean R, Stiufiuc RI, et al. Saturation of Specific Absorption Rate for Soft and Hard Spinel Ferrite Nanoparticles Synthesized by Polyol Process n.d. https://doi.org/10.3390/magnetochemistry6020023.

[29] Albino M, Fantechi E, Innocenti C, López-Ortega A, Bonanni V, Campo G, et al. Role of Zn2+ Substitution on the Magnetic, Hyperthermic, and Relaxometric Properties of Cobalt Ferrite Nanoparticles. The Journal of Physical Chemistry C 2019;123:6148–57. https://doi.org/10.1021/acs.jpcc.8b10998.

[30] Atif M, Turtelli R, Siddique M, Nadeem M. Effect of Mn substitution on the cation distribution and temperature dependence of magnetic anisotropy constant in Co1−xMnxFe2O4 (0.0≤x≤0.4) ferrites. Ceram Int 2014;40:471–8. https://doi.org/10.1016/j.ceramint.2013.06.026.

[31] Kambale RC, Shaikh PA, Harale NS, Bilur VA, Kolekar YD, Bhosale CH, et al. Structural and magnetic properties of Co1−xMnxFe2O4 (0 ≤ x ≤ 0.4) spinel ferrites

synthesized by combustion route. J Alloys Compd 2010;490:568–71. https://doi.org/10.1016/J.JALLCOM.2009.10.082.

[32] Yadav SP, Shinde SS, Bhatt P, Meena SS, Rajpure KY. Distribution of cations in Co1−xMnxFe2O4 using XRD, magnetization and Mössbauer spectroscopy. J Alloys Compd 2015;646:550–6. https://doi.org/10.1016/J.JALLCOM.2015.05.270.

[33] Szatmari A, Atanasov R, Barbu-Tudoran L, Nekvapil F, Dudric R, Tetean R. Enhanced Magnetic Properties of Co1−xMnxFe2O4 Nanoparticles 2024. https://doi.org/10.3390/app15010290.

[34] White WB, DeAngelis BA. Interpretation of the vibrational spectra of spinels. Spectrochim Acta A 1967;23:985–95. https://doi.org/10.1016/0584-8539(67)80023-0.

[35] Kim Y Il, Kim D, Lee CS. Synthesis and characterization of CoFe2O4 magnetic nanoparticles prepared by temperature-controlled coprecipitation method. Physica B Condens Matter 2003;337:42–51. https://doi.org/10.1016/S0921-4526(03)00322-3.

[36] Ansari SM, Ghosh KC, Devan RS, Sen D, Sastry PU, Kolekar YD, et al. Eco-Friendly Synthesis, Crystal Chemistry, and Magnetic Propertiesof Manganese-Substituted CoFe2O4Nanoparticles. ACS Omega 2020;5:21. https://doi.org/10.1021/acsomega.9b02492.

[37] P.V. Kovtunenko. Science For Ceramic Production Defect Formation In Oxygen Nonstoichiometric. Plenum Publishing Corporation 1997;54:9–15.

[38] Chakrabarty S, Dutta A, Pal M. Enhanced magnetic properties of doped cobalt ferrite nanoparticles by virtue of cation distribution. J Alloys Compd 2015;625:216–23. https://doi.org/10.1016/J.JALLCOM.2014.10.179.

[39] Fernandes C, Pereira C, Fernández-García MP, Pereira AM, Guedes A, Fernández-Pacheco R, et al. Tailored design of CoxMn1−xFe2O4 nanoferrites: a new route for dual control of size and magnetic properties. J Mater Chem C Mater 2014;2:5818–28. https://doi.org/10.1039/C4TC00429A.

[40] Botez CE, Adair AH, Tackett RJ. Evidence of superspin-glass behavior in Zn 0.5 Ni 0.5 Fe 2 O 4 nanoparticles. Journal of Physics: Condensed Matter 2015;27:076005. https://doi.org/10.1088/0953-8984/27/7/076005.

[41] Stoner EC, Wohlfarth EP. A mechanism of magnetic hysteresis in heterogeneous alloys. IEEE Trans Magn 1991;27:3475–518. https://doi.org/10.1109/TMAG.1991.1183750.

[42] Alzoubi GM, Masadeh AS, Shatnawi MTM. Investigation of the structural, morphological, and magnetic properties of small crystalline Co–Cu ferrite nanoparticles in the single-domain regime. AIP Adv 2022;12:065101. https://doi.org/10.1063/5.0087446.

[43] Ganguly S, Das P, Srinivasan S, Rajabzadeh AR, Tang XS, Margel S. Superparamagnetic Amine-Functionalized Maghemite Nanoparticles as a Thixotropy Promoter for Hydrogels and Magnetic Field-Driven Diffusion-Controlled Drug Release. ACS Appl Nano Mater 2024;7:5272–86. https://doi.org/10.1021/acsanm.3c05543.

[44] Klee A, Prevost S, Kunz W, Schweins R, Kiefer K, Gradzielski M. Magnetic microemulsions based on magnetic ionic liquids. Physical Chemistry Chemical Physics 2012;14:15355–60. https://doi.org/10.1039/C2CP43048G.

List of figures

List of tables